

Lateral phase separation in polymer-blend thin films: Surface bifurcation

Sam Coveney and Nigel Clarke

Department of Physics and Astronomy, University of Sheffield, Hicks Building, Hounsfield Road, Sheffield S3 7RH, United Kingdom

(Received 29 April 2014; published 23 June 2014)

We use simulations of a binary polymer blend confined between selectively attracting walls to identify and explain the mechanism of lateral phase separation via a transient wetting layer. We first show that equilibrium phases in the film are described by one-dimensional phase equilibria in the vertical (depth) dimension, and demonstrate that effective boundary conditions imposed by the film walls pin the film profile at the walls. We then show that, prior to lateral phase separation, distortion of the interface in a transient wetting layer is coupled to lateral phase separation at the walls. Using Hamiltonian phase portraits, we explain a “surface bifurcation mechanism” whereby the volume fraction at the walls evolves and controls the dynamics of the phase separation. We suggest how solvent evaporation may assist our mechanism.

DOI: [10.1103/PhysRevE.89.062603](https://doi.org/10.1103/PhysRevE.89.062603)

PACS number(s): 64.75.Va, 64.75.Cd, 64.75.St

I. INTRODUCTION

Understanding the mechanisms controlling phase separation in polymer-blend films is important for processing organic electronic devices such as polymer light emitting diodes and photovoltaic films, since film morphology is linked heavily to device performance. This work, which expands upon a recently published paper [1], identifies a different mechanism which explains the dynamics of lateral phase separation via a transient wetting layer. The distinction between the layered morphology of vertical phase separation (one phase in contact with a surface) and the nonwet morphology of lateral phase separation (both phases in contact with a surface) was recognized in early numerical studies of binary blends [2], with a high wall-field, low thermal noise regime corresponding to a layered morphology, and a low wall-field, high thermal noise regime corresponding to a partially wet morphology. The vertical layering of phases was realized both experimentally [3] and computationally [4,5], even in the nonwet regime when it is energetically favorable for both phases to be in contact with the surface [6,7]. Experiments later revealed that the vertical layers forming in the nonwet regime can break up as lateral structures appear at a surface [8]. The initial formation of a transient wetting layer (bilayer) which breaks up due to an instability has also received more recent attention [9,10]. Despite the recognition of these phenomena, the dynamics of the breakup of the transient wetting layer are not understood, nor is the fundamental mechanism underlying the dynamics. We use diffusion simulations of polymer-blend films confined between selectively attracting walls to identify the dynamics of lateral phase separation, using Hamiltonian phase portraits of one-dimensional (1D) phase equilibria to explain a “surface bifurcation mechanism” [11,12].

Sections IV–VII may be sufficient to understand our main result, since preceding sections are concerned mainly with theory. We proceed as follows: In Sec. II we revisit the problem of solving for 1D phase equilibria in binary polymer-blend films. In Sec. III we derive our diffusion equation. In Sec. IV we show that 1D phase equilibria (calculated in the vertical dimension perpendicular to the walls) can effectively describe both the vertically segregated (bilayer) and laterally segregated state, and we discuss exactly how

effective boundary conditions enforced by the film walls will pin the film profile at the walls. In Sec. V we show our diffusion simulations of lateral phase separation via a transient wetting layer (TWL) and explain this phenomenon using 1D phase equilibria. We argue that the growth of lateral inhomogeneities at the confining walls (bifurcation of the film profile at the walls, controlled by the wall boundary conditions) coincides with distortion of the interface in the unstable TWL: this causes the particular dynamics of lateral phase separation. In Sec. VI we compare our results with experiments involving solvent evaporation. We conclude in Sec. VII.

II. 1D PHASE EQUILIBRIA

The Flory–Huggins–de Gennes free energy functional \mathcal{F} for a 1D binary polymer blend (monodisperse, components A and B , volume fraction of A given by ϕ , depth d) confined between selectively attracting walls (surfaces) at $z = 0$ and $z = d$ is [13]

$$\mathcal{F}[\phi(z)] = \frac{1}{a} \int_0^d [f_{FH}(\phi) + \kappa(\phi)(\nabla\phi)^2] dz + f_0^*(\phi_0) + f_d^*(\phi_d), \quad (1)$$

where \mathcal{F} is given in units of $k_B T$, z measures the vertical distance from the wall at $z = 0$, and $\nabla\phi \equiv \partial_z\phi$ is the partial derivative of ϕ with respect to z . a is the spacing of the underlying Flory-Huggins lattice. To isolate the symmetry-breaking effects of the film walls, we restrict ourselves to a symmetric binary polymer blend (average composition $\bar{\phi} = 1/2$, degree of polymerization $N_A = N_B = N$), so the Flory-Huggins free energy contribution to Eq. (1) in units of $k_B T$ is

$$f_{FH} = \frac{\phi}{N} \ln(\phi) + \frac{1-\phi}{N} \ln(1-\phi) + \chi\phi(1-\phi), \quad (2)$$

where χ is the Flory-Huggins interaction parameter. The gradient coefficient $\kappa(\phi)$ in Eq. (1) is

$$\kappa(\phi) \equiv \kappa = \frac{a^2}{36\phi(1-\phi)}. \quad (3)$$

The (bare) surface energies f_0^* and f_d^* are given by [14,15]

$$\begin{aligned} f_S^*(\phi_S) &= h_S^* \phi_S + \frac{1}{2} g_S^* \phi_S^2 \\ &= \frac{1}{a} \left(h_S \phi_S + \frac{1}{2} g_S \phi_S^2 \right) \equiv \frac{1}{a} f_S(\phi_S), \end{aligned} \quad (4)$$

where $S = 0, d$ (the index S denotes the confining walls) and $h_S^* \equiv h_S/a$ and $g_S^* \equiv g_S/a$ are phenomenological parameters, taking account of blend-wall interactions and ‘‘missing neighbor’’ contributions due to the walls (surfaces), respectively. Only the local volume fraction ϕ_S enters into Eq. (4). Note that the definitions $f_S(\phi_S) = h_S \phi_S + \frac{1}{2} g_S \phi_S^2$ are the surface energies per unit cell. These are convenient because h_S and g_S are independent of the dimensionality \mathcal{D} of the system [which enters as $a^{-\mathcal{D}}$ in Eqs. (1) and (4)].

We will denote film profiles, describing the volume fraction ϕ as a function of distance z , by $\phi(z)$. In one dimension the total free energy is given by

$$\mathcal{F}_{TOT}[\phi(z)] = \mathcal{F}[\phi(z)] - \frac{\mu}{a} \int_0^d \phi(z) dz, \quad (5)$$

where a factor of $k_B T$ has been absorbed into the chemical potential μ . Equilibrium profiles (equilibria) $\phi(z)$ correspond to a minimum in the total free energy, i.e., $\delta \mathcal{F}_{TOT} / \delta \phi(z) = 0$, given equivalently by

$$\frac{\delta \mathcal{F}[\phi(z)]}{\delta \phi(z)} \equiv \frac{\mu(z)}{a} = \frac{\mu}{a}, \quad (6)$$

meaning that for equilibria $\phi(z)$ the local chemical potential $\mu(z)$ is a constant value μ for all z . Note that Eq. (6) contains a functional (variational) derivative. For any chosen blend ratio $A : B$ (quantified by the average composition $\bar{\phi}$) equilibria implied to exist in isolation (rather than coexisting with other phases) must conserve $\bar{\phi}$, which for a symmetric binary blend means $\bar{\phi} = 1/2$. In a laterally segregated film of coexisting phases $\phi_A(z)$ and $\phi_B(z)$ (rich in components A or B , i.e., $\bar{\phi}_B < \bar{\phi} < \bar{\phi}_A$), adjustment of the area and composition of each phase can conserve material.

We recently extended a Hamiltonian phase portrait method [11] to study a nontrivial problem, namely films of *finite* thickness with *asymmetrically* attracting surfaces (the use of phase portraits, such as in the seminal work by Pandit and Wortis [16], is discussed further in Ref. [12]). Our method allowed all equilibria to be identified, and their evolution through phase space tracked as film depth and temperature are changed. We will describe how to interpret Hamiltonian phase portraits in Sec. V. Here we will only show how a Lagrange multiplier is required to manipulate the phase portraits to obtain equilibrium profiles, and state the boundary conditions arising from the presence of confining walls. Underlying the Hamiltonian phase portrait method is the Euler-Lagrange equation. The Lagrangian density \mathcal{L} is the integrand of Eq. (1):

$$\mathcal{L}(\phi, \nabla \phi) = a^{-1} [f_{FH}(\phi) + \kappa(\phi)(\nabla \phi)^2]. \quad (7)$$

For a symmetric blend, a suitable constraint equation required for profiles which independently conserve material is

$$\frac{1}{a} \int_0^d \left(\phi(z) - \frac{1}{2} \right) dz = 0. \quad (8)$$

We choose the simple constraint $a^{-1} \phi$ and write a new Lagrangian \mathcal{L}' as follows:

$$\mathcal{L}' = \mathcal{L} + a^{-1} \lambda \phi. \quad (9)$$

λ is a Lagrange multiplier. The Euler-Lagrange equation for equilibrium profiles $\phi(z)$ is then

$$2\kappa \nabla^2 \phi - \partial_\phi \kappa (\nabla \phi)^2 = \partial_\phi f_{FH} + \lambda, \quad (10)$$

where ∂_ϕ is the partial derivative with respect to ϕ . Equation (10) is not enough to fully specify a solution; we require two boundary conditions to numerically solve for a unique solution. Setting the variational derivative of the total free energy (5) with respect to $\phi(z)$ to zero, we obtain two boundary conditions (written in terms of the dimension independent surface energies):

$$+ 2\kappa(\phi_0) \nabla \phi_0 = + \frac{\partial f_0}{\partial \phi} \equiv +h_0 + g_0 \phi_0, \quad (11)$$

$$+ 2\kappa(\phi_d) \nabla \phi_d = - \frac{\partial f_d}{\partial \phi} \equiv -h_d - g_d \phi_d. \quad (12)$$

The boundary conditions (11) and (12) must be satisfied, along with the constraint equation (8) via choice of λ , to specify equilibrium profiles $\phi(z)$ which also satisfy the Euler-Lagrange equation (10) [14,15,17].

III. DIFFUSION EQUATION

To derive our diffusion equation, we require the local chemical potential $\mu(z')$, given by the variational derivative of the free energy (1) at z' :

$$\mu(z') = a \frac{\delta \mathcal{F}[\phi(z)]}{\delta \phi(z')}. \quad (13)$$

We point out that Eq. (1) can be written as

$$\begin{aligned} a \mathcal{F}[\phi(z)] &= \int_0^d [f_{FH}(\phi) + \kappa(\phi)(\nabla \phi)^2 \\ &\quad + f_0(\phi) \delta_{z0} + f_d(\phi) \delta_{zd}] dz, \end{aligned} \quad (14)$$

where δ_{zS} represents the Kronecker δ function: $\delta_{zS}(z = S) = 1$, $\delta_{zS}(z \neq S) = 0$ (S refers to the value of z at the walls, i.e., $S = 0$ or $S = d$). The variational derivative in Eq. (13) describes how \mathcal{F} changes when we perturb the profile $\phi(z)$ by an infinitesimally small amount ϵ at the point $z = z'$:

$$\frac{\delta \mathcal{F}}{\delta \phi} = \lim_{\epsilon \rightarrow 0} \frac{1}{\epsilon} \{ \mathcal{F}[\phi(z) + \epsilon g(z, z')] - \mathcal{F}[\phi(z)] \}. \quad (15)$$

$g(z, z')$ is a test function (not rigorously a δ function or δ distribution) whose value is 0 for $z \neq z'$ and 1 for $z = z'$. It is necessary to use such a test function due to the finite range of the integral in the functional Eq. (14).

We will begin with the variational derivative of the gradient term $\kappa(\phi)(\nabla \phi)^2$ in Eq. (14). We use the contractions $g(z, z') \equiv g$ and $\kappa \equiv \kappa(\phi)$ when convenient, and discard all terms $O(\epsilon^2)$ in the expanded integrands since they vanish in the limit $\epsilon \rightarrow 0$. Note that the integrals vanish when we take $z' = z$ due to

the properties of the test function $g(z, z')$. We arrive at

$$\begin{aligned}
& \frac{1}{\epsilon} \int_0^d \kappa(\phi + \epsilon g) [\nabla(\phi + \epsilon g)]^2 - \kappa(\phi) [\nabla\phi]^2 dz \\
&= \int_0^d 2\kappa \nabla\phi \nabla g + g(\partial_\phi \kappa) (\nabla\phi)^2 dz \\
&= [2\kappa \nabla\phi g]_0^d - \int_0^d 2\kappa g \nabla^2 \phi dz \\
&\quad - \int_0^d 2\nabla\phi g \nabla\kappa dz + \int_0^d g(\partial_\phi \kappa) (\nabla\phi)^2 dz \\
&= [2\kappa \nabla\phi]_0^d - 2\kappa \nabla^2 \phi - 2\nabla\phi \nabla\kappa + (\partial_\phi \kappa) (\nabla\phi)^2 \\
&= [2\kappa \nabla\phi]_0^d - 2\kappa \nabla^2 \phi - (\partial_\phi \kappa) (\nabla\phi)^2. \tag{16}
\end{aligned}$$

The variational derivative of the Flory-Huggins free energy (2) is simply $\partial_\phi f_{FH}$, and the variational derivatives of the surface energies in Eq. (4) are $[\partial_\phi f_s(\phi)]_{\delta_{zS}}$. So we have for the local chemical potential $\mu(z)$ at point z

$$\begin{aligned}
\mu(z) &= -2\kappa(\phi) \nabla^2 \phi - (\partial_\phi \kappa) (\nabla\phi)^2 + \partial_\phi f_{FH} \\
&\quad + [+2\kappa(\phi) \nabla\phi + \partial_\phi f_d(\phi)]_{\delta_{zd}} \\
&\quad + [-2\kappa(\phi) \nabla\phi + \partial_\phi f_0(\phi)]_{\delta_{z0}}, \tag{17}
\end{aligned}$$

where the surface energy terms and $[2\kappa(\phi) \nabla\phi]_0^d$ have been combined, since both pairs of terms act at the walls [the terms $[2\kappa(\phi) \nabla\phi]_0^d$ are often missing from similar work in the literature].

Equation (6) means the chemical potential must be constant everywhere at equilibrium, $\mu(z) = \mu$. The Euler-Lagrange equation (10) must also be satisfied by equilibrium profiles $\phi(z)$. Substituting Eq. (10) into Eq. (17) we obtain for equilibrium

$$\begin{aligned}
\mu(z) &= -\lambda + [+2\kappa(\phi) \nabla\phi + \partial_\phi f_d(\phi)]_{\delta_{zd}} \\
&\quad + [-2\kappa(\phi) \nabla\phi + \partial_\phi f_0(\phi)]_{\delta_{z0}}, \tag{18}
\end{aligned}$$

which requires that the boundary conditions Eqs. (11) and (12) are naturally satisfied (not artificially enforced in the numerics). By adding the Lagrange multiplier in Eq. (9), we find that

$$\mu \equiv \mu_{sim} = -\lambda, \tag{19}$$

i.e., at equilibrium, the Lagrange multiplier is the negative of the chemical potential.

We assume the material current can be written as $J(z) = -M^* \nabla \delta \mathcal{F} / \delta \phi$ where M^* is the mobility, assumed to be constant for simplicity. From the continuity equation $\partial \phi / \partial t = -\nabla \cdot J$ we obtain

$$\frac{\partial \phi(z)}{\partial t} = \frac{M^*}{a} \nabla^2 \mu(z) \equiv M \nabla^2 \mu(z). \tag{20}$$

Inserting Eq. (17) into Eq. (20) gives us our diffusion equation. Scaling space by $z' = |\chi - \chi_S|^{1/2} z/a$ and time by $\tau = NM |\chi - \chi_S|^2 t/a^2$, and using the identity $\chi_C/2 = 1/N$ for a symmetric polymer blend (χ_C is the critical temperature of the blend and χ_S is the value of χ at the spinodal, which for a symmetric blend gives $\chi_S = \chi_C$) we

obtain

$$\begin{aligned}
\frac{\partial \phi(z)}{\partial \tau} &= \frac{1}{N} \nabla'^2 \left(\frac{1}{|\chi - \chi_S|} \frac{\partial f_{FH}}{\partial \phi} + \frac{(1-2\phi)\kappa}{\phi(1-\phi)a^2} (\nabla'\phi)^2 \right. \\
&\quad \left. - 2 \frac{\kappa}{a^2} \nabla'^2 \phi + \frac{\delta_{zd}}{|\chi - \chi_S|} \left[\frac{\partial f_d}{\partial \phi_d} + 2 \frac{|\chi - \chi_S|^{1/2}}{a} \kappa \nabla'\phi \right] \right. \\
&\quad \left. + \frac{\delta_{z0}}{|\chi - \chi_S|} \left[\frac{\partial f_0}{\partial \phi_0} - 2 \frac{|\chi - \chi_S|^{1/2}}{a} \kappa \nabla'\phi \right] \right), \tag{21}
\end{aligned}$$

where $\partial_\phi f_{FH} = (\chi_C/2) \ln(\phi/1-\phi) + \chi(1-\phi)$.

Equation (21) must be discretized for simulations (we use ‘‘simulation’’ throughout to mean numerically solving our resulting equation of motion). We divide the range in z by a mesh of D grid cells of depth Δz , so the film depth $d = D\Delta z$ and the surface terms act in the grid cells $i = 1$ and $i = D$ respectively. As first discussed by Henderson and Clarke [18], and later given firmer foundations by Fukuda *et al.* [19], inconsistencies can arise unless we normalize the surface (wall) energy (4) to make the free energy (14) invariant to the mesh size:

$$f_i(\phi_i) \rightarrow \frac{f_i(\phi_i)}{\Delta z} = \frac{h_i}{\Delta z} \phi_i + \frac{1}{2} \frac{g_i}{\Delta z} \phi_i^2, \tag{22}$$

where $i = 1$ or $i = D$. The surface gradient terms $\pm 2\kappa(\phi) \nabla\phi$ must also be normalized by Δz^{-1} , else the resulting discretized diffusion equation is not consistent with its continuous counterpart Eq. (21).

We also include a second lateral dimension y running parallel to the confining walls, using index j , and apply periodic boundary conditions in this dimension. The free energy functional (1) changes such that $a^{-1} \rightarrow a^{-2}$, but our careful definitions means that we need only replace factors of a^{-1} with a^{-2} in Secs. II and III [thus Eq. (19) remains unchanged]. We use a square simulation mesh $\Delta y = \Delta z$. Using ϕ_{ij} to represent the volume fraction of A at the grid cell ij , our 2D discrete diffusion equation is

$$\begin{aligned}
\frac{\partial \phi_{ij}}{\partial \tau} &= \frac{1}{N} \nabla'^2 \left(\frac{1}{|\chi - \chi_S|} \frac{\partial f_{FH}}{\partial \phi} \Big|_{ij} \right. \\
&\quad \left. + \frac{(1-2\phi_{ij})\kappa_{ij}}{\phi_{ij}(1-\phi_{ij})a^2} (\nabla'\phi|_{ij})^2 - 2 \frac{\kappa_{ij}}{a^2} \nabla'^2 \phi|_{ij} \right. \\
&\quad \left. + \frac{\delta_{iD}}{\Delta z'} \left[\frac{a^{-1}}{|\chi - \chi_S|^{1/2}} \frac{\partial f_d}{\partial \phi_d} + 2 \frac{\kappa_{Dj}}{a^2} \nabla'_z \phi|_{Dj} \right] \right. \\
&\quad \left. + \frac{\delta_{i1}}{\Delta z'} \left[\frac{a^{-1}}{|\chi - \chi_S|^{1/2}} \frac{\partial f_0}{\partial \phi_0} - 2 \frac{\kappa_{1j}}{a^2} \nabla'_z \phi|_{1j} \right] \right), \tag{23}
\end{aligned}$$

where $\kappa_{ij} \equiv \kappa(\phi_{ij})$ and $\partial_\phi f_{FH}|_{ij} \equiv \partial_\phi f_{FH}(\phi_{ij})$. The gradient terms ∇' and ∇'^2 are now 2D, while $\nabla'_z \equiv \partial'_z$. For the surface terms $\partial f_d / \partial \phi_d$ and $\partial f_0 / \partial \phi_0$, we have kept the notation for the continuous spatial variable z (0 and d), although these terms must be evaluated for grid cells with $i = 1, D$. (Note that the lattice spacing a cannot be scaled out of the surface terms; see Ref. [19].)

We make the film walls (surfaces) impenetrable, so material conservation is required,

$$\frac{d}{d\tau} \int_0^d \phi(z) dz = 0, \tag{24}$$

and implemented by a no-flux condition at the walls. To discretize Eq. (23), we use a central differencing scheme for space and a forward differencing time step:

$$\phi_{ij}^{\tau+\Delta\tau} = \phi_{ij}^{\tau} + \Delta\tau \frac{\partial\phi_{ij}}{\partial\tau}. \quad (25)$$

IV. 1D EQUILIBRIA IN 2D FILMS

Throughout this paper, we use a symmetric polymer blend $\bar{\phi} = 0.5$ with $N = 100$, hence $\chi_c = 0.020$. We use the following wall parameters and terminology: for “asymmetric” films $h_0 = -0.05$, $g_0 = 0.18$, $h_d = g_d = 0$ (a B -attracting wall at $z = 0$ and a neutral wall at $z = d$); for “antisymmetric” films $h_0 = -0.05$, $g_0 = 0.18$, $h_d = -0.13$, $g_d = 0.18$ (a B -attracting wall at $z = 0$ and an A -attracting wall at $z = d$, such that the walls attract opposite components in exactly the same way); and for “symmetric” films $h_0 = h_d = -0.05$, $g_0 = g_d = 0.18$ (a B -attracting wall at $z = 0$ and $z = d$). Simulations are started seeded with initial random noise, i.e., $\phi(z, y) = 0.5 + \delta\phi$, where $\delta\phi$ is chosen from a Gaussian distribution with mean zero and width σ , which will be specified. We show a simulation with noise in Sec. VIA (Fig. 19) to prove that our results are general. Since scaled space depends on the temperature χ , we discuss our results in terms of unscaled space z (in units implied by the Hamiltonian method of Ref. [11]) and scaled time τ .

Since the wetting temperature depends on the film thickness and wall interactions, we have defined the wetting temperature χ_w throughout as the cutoff temperature at which spontaneous lateral phase separation of a transient wetting layer no longer appears to occur (i.e., the wetting layer is stable, and the contact angle of the wetting phase with the surface remains zero) for an asymmetric film of depth $d = 20.1$ (the film depth used in Sec. V). This gives an estimate of $0.0213 < \chi_w < 0.0214$ (this provides an upper limit for all of our wall configurations, since our asymmetric configuration has one neutral wall; see Ref. [20]).

A. Laterally homogeneous films

To study laterally homogeneous films we restrict ourselves to asymmetric films, use quasi-1D simulations in which the lateral dimension y is too narrow to support laterally segregated states, and use $\sigma = 0.0001$ for a nearly homogeneous initial film. These quasi-1D simulations are directly comparable with calculated 1D film profiles. We studied three different temperature regimes: above the critical temperature $\chi = 0.015$ (Fig. 1), below the critical temperature but above the wetting temperature $\chi = 0.021$ (Fig. 2), and below the wetting temperature $\chi = 0.026$ (Fig. 3).

In Figs. 1–3 the three subfigures show each film at a very early time (a), an intermediate time (b), and at equilibrium (c). Animations are available in the Supplemental Material [21]. The data points ϕ_i ($1 \leq i \leq D$) are averages of ϕ_{ij} taken over index j (the lateral dimension) for fixed index i , and the dashed lines are the 1D equilibrium profiles of asymmetric films calculated by a Hamiltonian method. We make the following observations: at equilibrium the simulation data match the profiles; the simulations reproduce the profiles more accurately as the mesh size is reduced ($\Delta\tau = 0.00004$ was used for each temperature regime); and as $\Delta z \rightarrow 0$, the simulation data

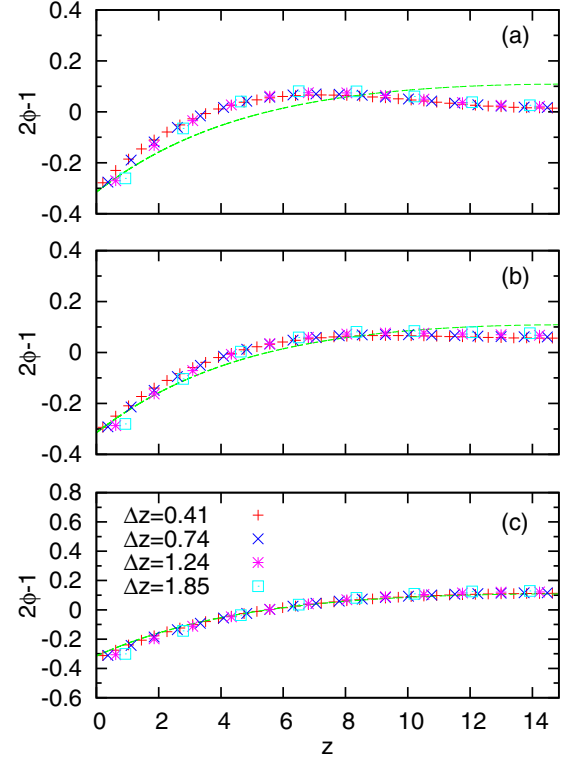


FIG. 1. (Color online) 1D simulation data for $\chi = 0.015$ ($\chi < \chi_c$), film depth $d = 14.85$, and asymmetric walls. Times are $\tau = 1$ (a), $\tau = 2$ (b), $\tau = 15$ (c). The calculated equilibrium profile (green dashed line) required $\lambda = -0.000745$, while $\mu_{sim} = +0.000791$ for $\Delta z = 0.41$. Equilibrium is a monolayer with positive adsorption of B material at the B attracting wall ($z = 0$).

conform exactly to the calculated profiles. Further proof of this is shown in Table I, which shows that as $\Delta z \rightarrow 0$ the simulation equilibrium chemical potential converges to the negative of the Lagrange multiplier required to numerically solve for the film profile, as predicted by Eq. (19) (these finer Δz are absent in Figs. 1–3 to preserve clarity).

B. Pinning of profiles at the walls

From Figs. 1–3 we see, in agreement with the literature [7], that the value of ϕ at the B -attracting wall appears to be very quickly pinned to its equilibrium value, and from this pinning center a concentration wave is crossing the film. On the other hand, the profile near the neutral wall is unperturbed at very early times, and it would appear that there is no such rapid pinning of ϕ at the neutral wall. For each temperature regime, a point is reached when the concentration wave has crossed the film, and the profiles show a monotonous increase in B towards the B attracting wall at $z = 0$ and flat profile at $z = d$. For Fig. 3, the film then develops nonmonotonous behavior at $z \approx 2.5$ (characterized by a minimum in ϕ near but not at the B -attracting wall) shortly prior to achieving metastable equilibrium.

A more careful inspection of the diffusion equation (23) and boundary conditions (11) and (12) shows us that the profile is in fact pinned at both the B -attracting wall and the neutral wall, but that “pinning” does not refer to just the volume fraction ϕ ,

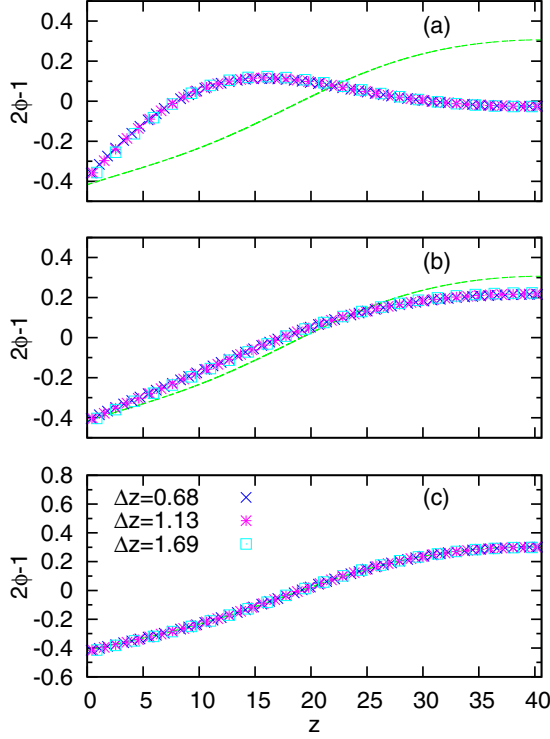


FIG. 2. (Color online) 1D simulation data for $\chi = 0.021$ ($\chi_C < \chi < \chi_W$), film depth $d = 40.60$, and asymmetric walls. Times are $\tau < 1$ (a), $\tau = 9$ (b), $\tau = 25$ (c). The calculated equilibrium profile (green dashed line) required $\lambda = -0.000\,033$, while $\mu_{sim} = +0.000\,036$ for $\Delta z = 0.68$. Equilibrium is a bilayer with a soft interface separating the B -rich phase and A -rich phase.

but rather to both coordinates $(\phi, 2\kappa \nabla \phi)$. The surface terms of the diffusion equation (23) effectively enforce the boundary conditions (11) and (12) such that they are fulfilled at all times during the simulation, not only at equilibrium. For the B -attracting wall, although ϕ is pinned at early times, it in fact does continue to change slightly, as does $\nabla \phi$. For the neutral wall, Eq. (12) with $h_d = g_d = 0$ shows us that $\nabla \phi = 0$ solves the boundary condition for any value of ϕ , so although the value of ϕ does not appear to be pinned, $\nabla \phi$ is pinned to zero. The wall-blend interactions thus enforce the boundary conditions at all times, but $(\phi, 2\kappa \nabla \phi)_{0,d}$ may still change while satisfying these boundary conditions. This observation will be important to our discussion of lateral phase separation in Sec. V, in which a graphical interpretation of this pinning can be made by considering phase portraits: no matter how the trajectories of the film profiles change during film evolution, the ends of the trajectories are always pinned to the boundary conditions (11) and (12).

C. Laterally segregated films

We now discuss 2D simulations at $\chi > \chi_W$, for which global equilibrium is a laterally segregated film. We will reserve discussion of the dynamics of lateral phase separation for Sec. V, and focus here on showing that the coexisting equilibria that can be calculated in one dimension (in the dimension running between the walls) do in fact occur in laterally segregated 2D films. Figures 4 and 5 show, for

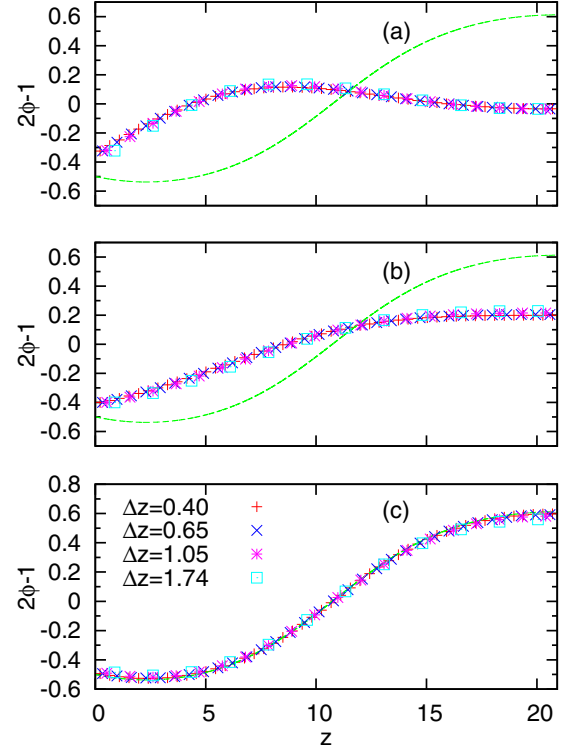


FIG. 3. (Color online) 1D simulation data for $\chi = 0.026$ ($\chi_W < \chi$), film depth $d = 20.92$, and asymmetric walls. Times are $\tau = 2$ (a), $\tau = 20$ (b), $\tau = 100$ (c). The calculated equilibrium profile (green dashed line) required $\lambda = +0.000\,120$, while $\mu_{sim} = -0.000\,118$ for $\Delta z = 0.40$. The equilibrium profile is nonmonotonous with a minimum ($\nabla \phi = 0$) at $z \approx 2.5$.

an asymmetric and a symmetric film respectively, only the laterally segregated state corresponding to global equilibrium, which should technically consist of only a single pair of coexisting phases in contact. We previously argued, on the

TABLE I. Lagrange multiplier λ (for the calculated 1D profile) and equilibrium chemical potential μ_{sim} (obtained from simulations) for different temperature regimes χ , depths d , and varying mesh size Δz (including all the data from the simulations for Figs. 1–3). As the mesh size becomes finer $\Delta z \rightarrow 0$, we observe $\mu \rightarrow -\lambda$, as predicted by Eq. (19). The rate equation (23) is therefore accurate and precise.

χ	λ	d	Δz	μ_{sim}
0.015	−0.000745	14.85	0.10	+0.000745
			0.41	+0.000791
			0.74	+0.000832
			1.24	+0.000897
0.021	−0.000033	40.60	1.85	+0.000985
			0.25	+0.000033
			0.68	+0.000036
0.026	+0.000120	20.92	1.13	+0.000037
			1.69	+0.000039
			0.40	−0.000120
			0.65	−0.000116
			1.05	−0.000112
			1.74	−0.000101

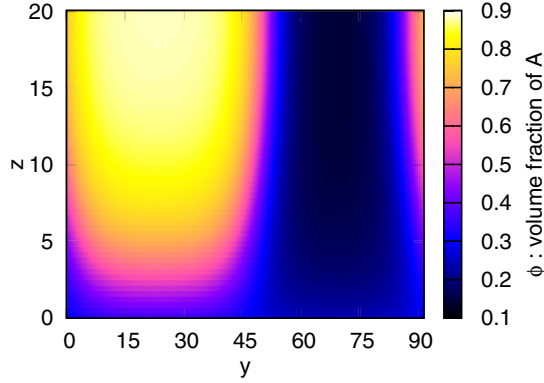


FIG. 4. (Color online) The laterally segregated state for $\chi = 0.026$ ($\chi > \chi_w$), depth $d = 20.1$, and asymmetric walls, using $\Delta z = 0.36$ and $\Delta \tau = 0.10 \times 10^{-5}$. The lateral dimension $y \approx 90$ (with periodic boundary conditions) is wide enough to support two lateral phases.

subject of solving for these coexisting phases in one dimension, that since a Lagrange multiplier $\lambda \neq 0$ always acts to increase the free energy of a profile relative to the same profile for $\lambda = 0$ (“same profile” in this context means that the solution trajectory through phase space is qualitatively the same, except for distortion due to a nonzero λ ; see Sec. V) that the coexisting solutions should be calculated in one dimension for $\lambda = 0$ [11]. Since actual coexistence of these lateral phases in a 2D film requires an interface we should expect $\lambda_A = \lambda_B \neq 0$ in general.

To compare the 2D simulation data of Figs. 4 and 5 with the 1D coexisting phases calculated via a 1D Hamiltonian method (requiring a choice of λ and Hamiltonian \mathcal{H} , explained in Sec. V), we took 1D cross sections of the 2D data at points at y_A and y_B , which are at the cores or centers of the *A*-rich and *B*-rich phases respectively. The cross sections from the asymmetric film of Fig. 4 ($y_A \approx 20$ and $y_B \approx 70$) are shown in Fig. 6, which also contains two pairs of curves. The curves to which no data points are directly aligned were obtained from a 1D calculation of the lateral phases using $\lambda = 0$. However,

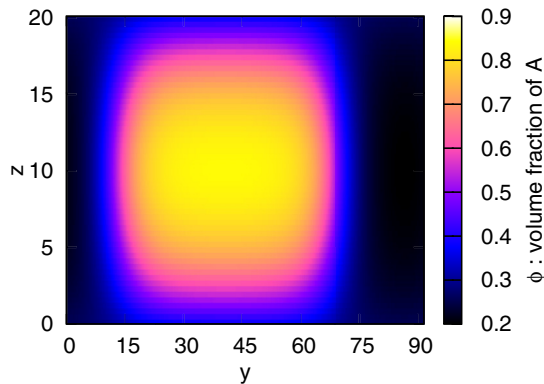


FIG. 5. (Color online) The laterally segregated state for $\chi = 0.026$ ($\chi > \chi_w$), depth $d = 20.1$, and symmetric walls, using $\Delta z = 0.36$ and $\Delta \tau = 0.25 \times 10^{-5}$. The lateral dimension $y \approx 90$ (with periodic boundary conditions) is wide enough to support two lateral phases.

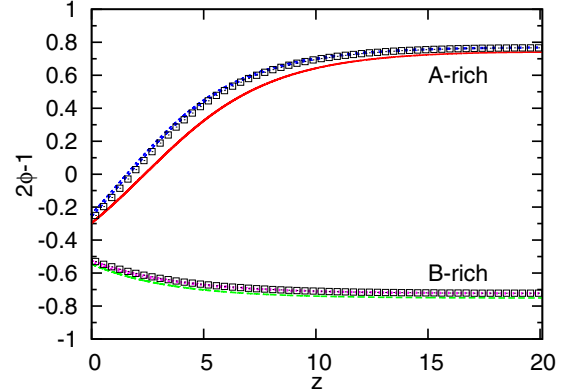


FIG. 6. (Color online) 1D vertical cross sections from Fig. 4 (data points), and calculated profiles (curves) of coexisting phases for $\chi = 0.026$ ($\chi > \chi_w$), depth $d = 20.1$, and asymmetric walls. The curves matching the data points (blue and pink) were calculated with $\lambda = -\mu_{sim} = -0.000491$ ($\mathcal{H}_A = 0.001357$, $\mathcal{H}_B = 0.000988$), while the other curves (red and green) were calculated with $\lambda = 0$ ($\mathcal{H}_A = 0.000923$, $\mathcal{H}_B = 0.000924$).

the simulation for Figs. 4 and 6 gave $\mu_{sim} = 0.000491$, so it is unsurprising that the data and the 1D calculated profiles do not coincide. The second set of curves, which are almost obscured by the data points, are the 1D profiles calculated with Lagrange multiplier $\lambda = -\mu_{sim} = -0.000491$. These 1D cross sections, while describing the majority of the cores of the phases very accurately, do not of course describe the interface between the phases. The cross-sectional profiles obtained from the data for the symmetric film of Fig. 5 ($y_A \approx 40$ and $y_B \approx 86$) are shown in Fig. 7, along with 1D coexisting phases calculated for $\lambda = -\mu_{sim} = -0.001202$ (a pair of *A*-rich and *B*-rich coexisting phases of depth $d = 20.1$ cannot be calculated for $\lambda = 0$). The relatively steep gradients in the *A*-rich phase cause some minor discretization errors, causing the *B*-rich phase of the symmetric film to be slightly less *B*-rich than expected. No data are shown for

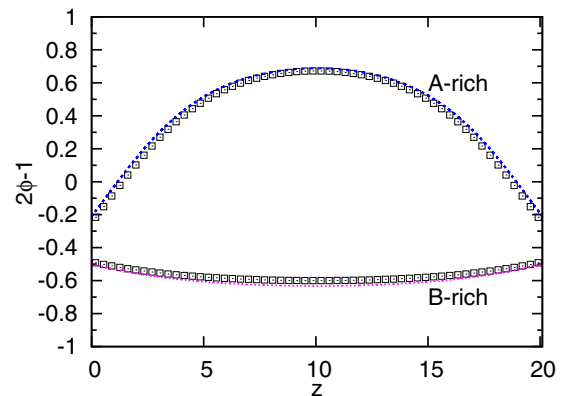


FIG. 7. (Color online) 1D vertical cross sections from Fig. 5 (data points), and calculated profiles (curves) of coexisting phases for $\chi = 0.026$ ($\chi > \chi_w$), depth $d = 20.1$, and symmetric walls. The calculated profiles required $\lambda = -\mu_{sim} = -0.001202$ ($\mathcal{H}_A = 0.001922$, $\mathcal{H}_B = 0.001092$). It is not possible to obtain *A*-rich profiles of depth $d = 20.1$ for $\lambda = 0$.

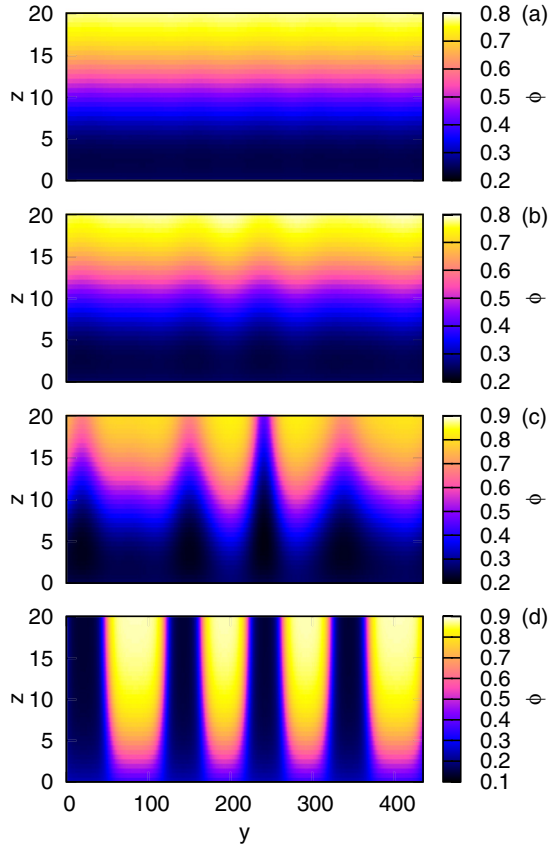


FIG. 8. (Color online) Simulation snapshots for $\chi = 0.026$ ($\chi > \chi_w$), $d = 20.1$ and asymmetric walls ($\Delta z = 0.50$, $\Delta\tau = 1.0 \times 10^{-5}$). (a) Metastable bilayer state with minor lateral inhomogeneities ($\tau = 100$); (b) distortion of bilayer interface with corresponding inhomogeneities at the walls ($\tau = 892$); (c) breakup of the bilayer interface as a column of B -rich material reaches the $z = d$ wall ($\tau = 1665$); (d) stable laterally segregated coexisting states ($\tau = 3655$).

antisymmetric films, since in this special case $\lambda = -\mu_{sim} = 0$, and so we find that the lateral interfaces between the perfectly antisymmetric 1D phases do not introduce a nonzero chemical potential. We conclude that the laterally segregated state is effectively described by 1D equilibria in the dimension running perpendicular to the confining walls.

V. BREAKUP OF WETTING LAYER

Figures 8, 10, 12, 14, and 16 show, for $\chi > \chi_w$, simulation snapshots of films undergoing lateral phase separation via a transient wetting layer. Animations of our 2D simulations are available in the Supplemental Material [21]. The width of the initial noise $\delta\phi$ was $\sigma = 0.05$, this choice allowing both the TWL and laterally segregated state to be probed. It is important to highlight here that the absence of a random noise term in our current model means that the final lateral states we present do not always consist of “wide” lateral phases (resulting from the merging of narrower lateral phases, for example) which are closer to “true” global equilibrium (a single pair of laterally coexisting phases). However, the distinction between multiple lateral phases (wide or narrow) and a single pair of laterally coexisting phases is of little practical relevance

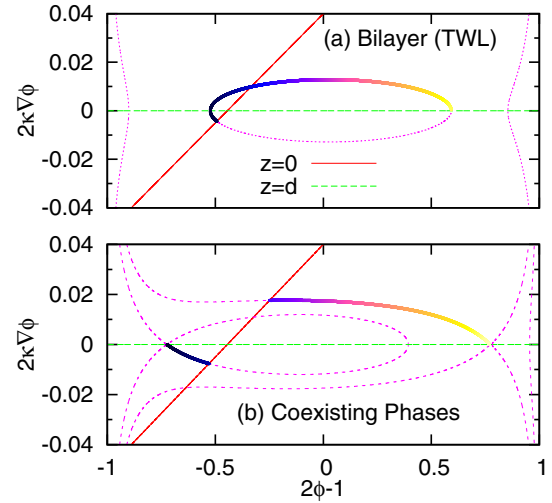


FIG. 9. (Color online) 1D phase portraits for equilibria in Fig. 8 (asymmetric walls). (a) Metastable bilayer (TWL) ($\lambda = +0.000119$, $\mathcal{H} = 0.000743$); (b) Coexisting phases ($\lambda = -\mu_{sim} = -0.000497$): A -rich phase ($\mathcal{H}_A = 0.001362$) and B -rich phase ($\mathcal{H}_B = 0.000989$). ϕ_d of all three phases are rather distinct. ϕ_0^{TWL} and ϕ_0^B are quite similar, but both distinct from ϕ_0^A .

to the mechanism we discuss here, or to most experiments. The lateral phases that appear in our simulations are the same phase equilibria that correspond to global equilibrium, and we refrain from using the latter term only because it could possibly be misleading (coarsening of the lateral phases in our simulations is technically possible). We present a simulation in which continuous random noise was included in Sec. VIA (Fig. 19), which shows that our results still hold in the case of continuous noise, and that wider lateral phases form in that case.

In this section, we make use of Hamiltonian phase portraits, Figs. 9, 11, 13, 15, and 17, to discuss the 1D phase equilibria [11,12]. For this system, Hamiltonian phase portraits consist of the flow of canonical coordinates $(\phi, 2\kappa\nabla\phi)$ which minimize the bulk free energy functional \mathcal{F} . The satisfied boundary conditions enforced by the walls [Eqs. (11) and (12)] are therefore represented by straight lines, since the boundary conditions pin $(\phi, 2\kappa\nabla\phi)$ at the walls. The solution “trajectories” are those parts of the phase portraits which flow between the wall boundary conditions. The phase portraits (which are symmetric around $\phi = 0.5$ for a symmetric blend if $\lambda = 0$) are distorted by the Lagrange multiplier $\lambda \neq 0$, which is a chemical potential. Suitable choices of both λ and the Hamiltonian constant \mathcal{H} (these sensitive parameters will be given to six decimal places) are necessary to produce phase equilibria trajectories of specified depth d and average composition $\bar{\phi}$. The phase portraits themselves provide significant insight, as the evolution of trajectories can be tracked graphically as depth, temperature, and wall interaction parameters change. Most importantly, we must understand that the ends of the trajectories are always pinned to the boundary conditions (even out of equilibrium, as shown in Sec. IV B). This is why bifurcation of the profile at the walls is inherent in lateral phase separation. We will denote the profile value of the TWL at the $z = 0$ wall by $(\phi, \nabla\phi)_0^{TWL}$, and similarly for other cases. To

assist in reading the phase portraits, we have colored (shaded) the trajectories to match the color range for ϕ shown in the simulation figures. Note that as χ increase, the bilayer interface sharpens. For $\chi < \chi_w$, this interface is rather diffuse, and the bilayer is stable against lateral phase separation, since a configuration of coexisting phases no longer has a lower free energy than the bilayer phase.

The wall configuration of the asymmetric film (a B -attracting wall and a neutral wall) is a special case in that there is only one surface field. This particular case (used as the example in our recent paper [1]) highlights the qualitatively different behavior at each confining surface and does not include any convenient symmetries that fix the chemical potential [e.g., $\mu(z) = 0$ for antisymmetric films]. General asymmetry complicates our discussions of the phase portrait method and would leave us short of discussing behavior at a neutral wall. However, a neutral wall is nonetheless a special case, and so after discussing asymmetric films in Sec. V A we will extend our discussion to two nonzero surface fields in Sec. V B.

A. One surface field

Figures 8, 10, and 12 are snapshots from 2D simulations at $\chi > \chi_w$ for $\chi = 0.026$, $\chi = 0.023$, and $\chi = 0.022$ respec-

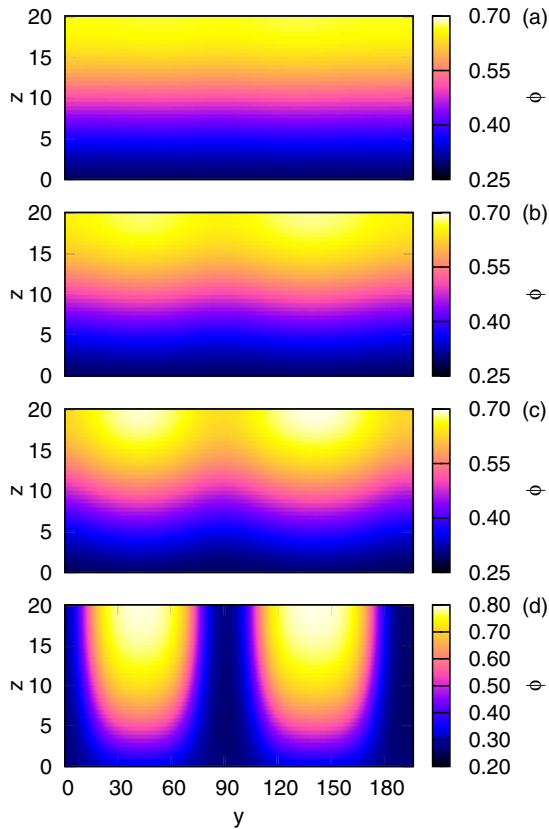


FIG. 10. (Color online) Simulation snapshots for $\chi = 0.023$ ($\chi > \chi_w$), $d = 20.1$, and asymmetric walls ($\Delta z = 0.50$, $\Delta \tau = 0.5 \times 10^{-5}$). (a) Metastable bilayer state ($\tau = 200$); (b) distortion of bilayer interface as lateral structures grow primarily at $z = d$ wall ($\tau = 550$); (c) A -rich phases growing from $z = d$ surface ($\tau = 700$); (d) stable laterally segregated coexisting states ($\tau = 1500$).

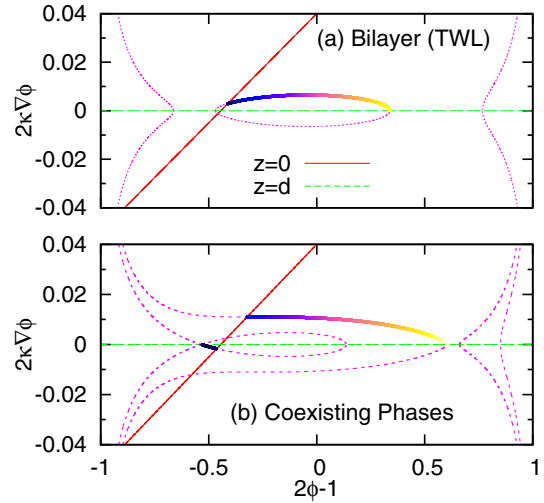


FIG. 11. (Color online) 1D phase portraits for equilibria in Fig. 10 (asymmetric walls). (a) Metastable bilayer (TWL) state ($\lambda = -0.000113$, $\mathcal{H} = 0.001332$), with two crosses of the $z = 0$ boundary condition (BC) along the flow; (b) coexisting phases ($\lambda = -\mu_{sim} = -0.000367$): A -rich phase ($\mathcal{H}_A = 0.001618$) and B -rich phase ($\mathcal{H}_B = 0.001404$). ϕ_d (ϕ_0) of all three phases are rather distinct (similar).

tively, for asymmetric films of depth $d = 20.1$, showing direct observations of lateral phase separation via a transient wetting layer. Time increases from subfigures (a) to (d). In all cases the film first evolves into a bilayer (vertically stratified) state, which is the TWL, and this bilayer subsequently breaks up into laterally segregated states. Figures 9, 11, and 13 show 1D phase equilibria ($d = 20.1$) in Hamiltonian phase space for the phases that form in Figs. 8, 10, and 12 respectively.

Figures 8(a), 10(a), and 12(a) all show a “bilayer” state with a B -rich (A -rich) phase coating the B -attracting (neutral) wall, respectively, and a “soft” interface separating these phases [22] (for comparison, Figs. 2 and 3 are both bilayer profiles, while the profile of 1 is a monolayer with positive adsorption of B at the B -attracting wall at $z = 0$). Figures 9(a), 11(a), and 13(a) show, in phase space, the independently existing solution of lowest free energy (a bilayer), λ having been chosen to ensure $\bar{\phi} = 1/2$. The average chemical potential of the bilayer state in Figs. 8, 10, and 12 (the average is over all grid cells) confirm that the films are in the 1D metastable bilayer states shown in the phase portraits of Figs. 9(a), 11(a), and 13(a) (e.g., for $\chi = 0.026$, $\langle \mu_{sim} \rangle = 0.000112$, while $-\lambda = 0.000119$ for the calculated profile).

Figures 8, 10, and 12 show that lateral inhomogeneities in the bilayer state continue to grow with time and the interface separating the phases of the bilayer becomes distorted [subfigures (b)]. Any distortion of the interface appears to correspond to lateral inhomogeneities which have appeared at the confining walls, most notably at the neutral wall at $z = d$. The average chemical potential remains approximately that of the bilayer during this distortion, and only when the interface appears to break up does the average chemical potential begin to rapidly change, indicating that the film is now in the process of leaving its long-lived metastable equilibrium. At later times [subfigures (c)] the interface breaks up: Fig. 8(c) shows the

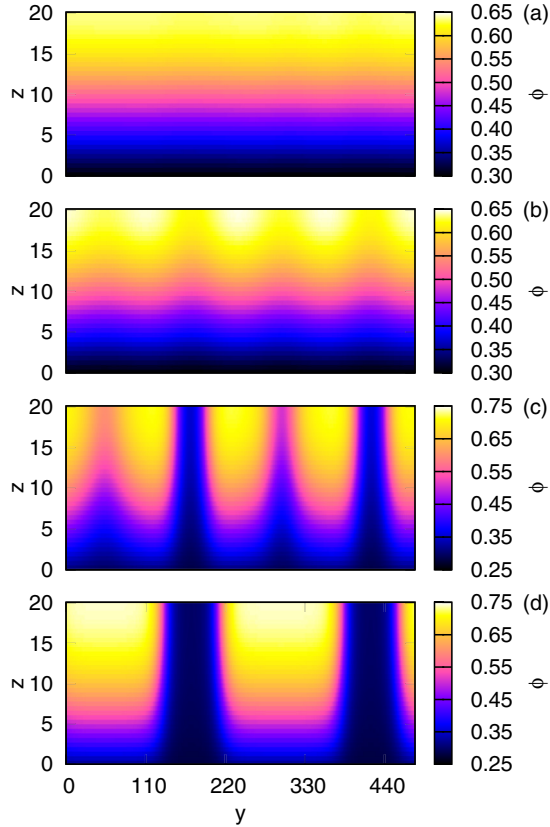


FIG. 12. (Color online) Simulation snapshots for $\chi = 0.022$ ($\chi > \chi_w$), $d = 20.1$, and asymmetric walls ($\Delta z = 0.56$, $\Delta\tau = 0.25 \times 10^{-5}$). (a) Metastable bilayer state ($\tau = 100$); (b) late stages of bilayer state with visible change of ϕ at the $z = d$ wall ($\tau = 1000$); (c) merging of adjacent growing A -rich lateral phases at around $y \approx 50$ and $y \approx 300$ ($\tau = 1800$); (d) stable laterally segregated coexisting states ($\tau = 4000$).

interface moments after a column of B -rich material reaches the $z = d$ surface; Fig. 10(c) shows the interface just prior to breakup, showing significant variations in ϕ_d ; and Fig. 12(c) shows the film after the breakup of the interface as some lateral phases merge to reduce interfacial energy. It can be seen that points where the interface touches down on the walls and where the lateral phases develop from are exactly the same points where the initial lateral variations at the walls took place, and in fact it appears that the A -rich phases are growing from the neutral wall at $z = d$. The final states [subfigures (d)] of Figs. 8, 10, and 12 show the film in the laterally segregated state, and it is clear that the lateral phases have formed exactly where the initial lateral variations at the walls took place. This strongly suggests that the wall-blend interactions are controlling the dynamics of lateral phase separation.

Figures 9(b), 11(b), and 13(b) are phase portraits of the A -rich and B -rich laterally coexisting phases respectively, calculated using the chemical potentials extracted from the simulations $\lambda = -\mu_{sim}$ when the film has achieved a static laterally segregated state. The phase portraits describe the profiles from the simulations exactly, and clearly show how the profiles evolve as χ is changed, including the increased homogeneity of the B -rich phase as $\chi = 0.026 \rightarrow 0.023$ and

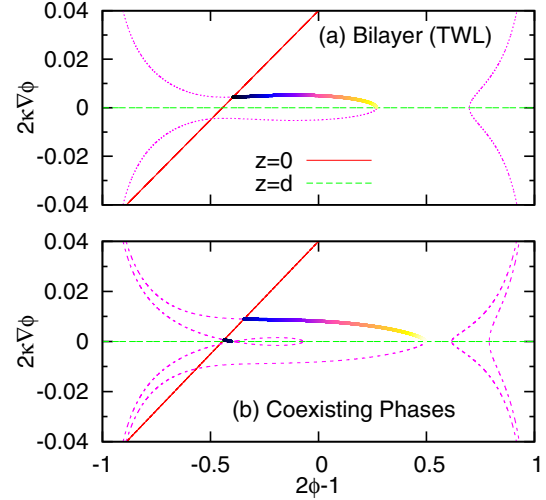


FIG. 13. (Color online) 1D phase portraits for equilibria in Fig. 12 (asymmetric walls). (a) Metastable bilayer (TWL) ($\lambda = -0.000184$, $\mathcal{H} = 0.001580$); (b) coexisting phases ($\lambda = -\mu_{sim} = -0.000333$): A -rich phase ($\mathcal{H}_A = 0.001747$) and B -rich phase ($\mathcal{H}_B = 0.001589$). The B -rich trajectory shows $\phi_B \equiv 1 - \phi$ increases towards the $z = 0$ wall, which was not the case for Figs. 8 and 10. ϕ_d (ϕ_0) of all three phases are rather distinct (similar).

a qualitative change in the B -rich solution for $\chi = 0.023 \rightarrow 0.022$ as the B -attracting wall becomes richer in B material than elsewhere in the B -rich phase. Previous work in one dimension has already shown that a bilayer state is unstable with respect to a laterally segregated state due to having a greater free energy [11,12], and it is now apparent that the result carries across to two dimensions. We conclude that the transient wetting layer, which initially forms due to preferential attraction by the confining walls, breaks up because it is metastable with respect to the laterally segregated state. The intrinsic instability of the transient wetting layer as a whole is different from an instability in the interface between the vertically segregated phases of the bilayer. We expand on this point presently, using the phase portraits Figs. 9, 11, and 13 to explain the dynamics of the film evolution.

For $\chi = 0.022$, Fig. 13 shows that the trajectory (colored part of the phase portrait) of the TWL passes through each boundary condition only once (although the Hamiltonian flow crosses each boundary condition twice, in the region of interest) and the same is true for the A -rich and B -rich trajectories, which flow between crosses similar to that of the TWL. In this case, we see that $|\phi_0^A - \phi_0^B| \ll |\phi_d^A - \phi_d^B|$ (ϕ_d is quite different for the coexisting phases, unlike ϕ_0) and $|\phi_0^{TWL} - \phi_0^A| \ll |\phi_d^{TWL} - \phi_d^A|$, which means that for the A -rich phase to form, ϕ_d must change by much more than ϕ_0 . As Fig. 12 shows, lateral phase separation happens as the A -rich lateral phases appear to grow from the $z = d$ wall. For $\chi = 0.023$, even though the B -rich trajectory exists on a different region in the phase space [the closed tear-shaped loop in Fig. 11(b)] such that the “bulk” of the profile is slightly different, Fig. 10 shows that the lateral phases still appear to grow from the $z = d$ surface, since the same arguments as for the previous case can be made. For $\chi = 0.026$, Fig. 9 shows

that the TWL trajectory crosses each boundary condition twice, and each coexisting phase flows between a different cross of the flow with the boundary conditions. ϕ_0 and ϕ_d for both the A-rich and B-rich phases differ much more from $\phi_{0,d}^{TWL}$ than in the case of $\chi = 0.022$. This is especially true of ϕ_0^A . Figure 8 shows that the breakup of the interface is due to significant variations in ϕ at both confining walls, the largest variations in ϕ_0^{TWL} of the bilayer being precisely where the columns of A-rich phase form. This is expected from inspection of Fig. 9, which shows that ϕ_0^{TWL} and ϕ_0^B are still fairly similar, but ϕ_0^A of the A-rich phase is significantly different from both those values. The column of B-rich phase reaches the $z = d$ surface when ϕ_d , which had been gradually change during the interface distortion, suddenly undergoes a quick transient $\phi_d^{TWL} \rightarrow \phi_d^B$ as the interface appears to reach the surface and break. The phase portraits thus offer practical insight into the dynamics of the breakup of the transient wetting layer.

The simulations of Figs. 8, 10, and 12 seem to show that the breakup of the bilayer state proceeds from the neutral wall at $z = d$. Since the profiles are pinned to the boundary conditions at all times, lateral phase separation clearly requires

that the single value of the volume fraction at each wall must undergo a bifurcation into two values: $\phi_{0,d}^{TWL} \rightarrow \phi_{0,d}^A, \phi_{0,d}^B$, the bifurcation at the $z = d$ wall being much more pronounced for asymmetric films (clearly, due to the interface between the coexisting phases, there are more than two values at the wall, but it is much simpler to discuss the coexisting states in terms of the 1D phase equilibria). Note that this “surface bifurcation” is technically $(\phi, 2\kappa \nabla \phi)_{0,d}^{TWL} \rightarrow (\phi, 2\kappa \nabla \phi)_{0,d}^A, (\phi, 2\kappa \nabla \phi)_{0,d}^B$ but it is sufficient here to discuss only $\phi_{0,d}$ (which can be experimentally measured). The distortion of the interface in the TWL is coupled to phase separation at the walls due to the boundary conditions enforced by the walls.

B. Two surface fields

Figure 14 shows snapshots from simulations of a polymer blend between antisymmetric confining walls. As in the case of asymmetric confinement, a bilayer state (TWL) first forms which subsequently breaks up to give a laterally segregated state. The Hamiltonian flow containing the bilayer trajectory, shown in Fig. 15(a), is very similar to the flow in Fig. 9(a). Figure 15(a) shows that the TWL trajectory passes through $\nabla \phi = 0$ (stationary points) near each wall, with a corresponding maximum in $\phi_A \equiv \phi$ ($\phi_B \equiv 1 - \phi$) near the A-attracting (B-attracting) wall. Figure 14 shows that the distortion of the interface in the bilayer appears to be caused by growing

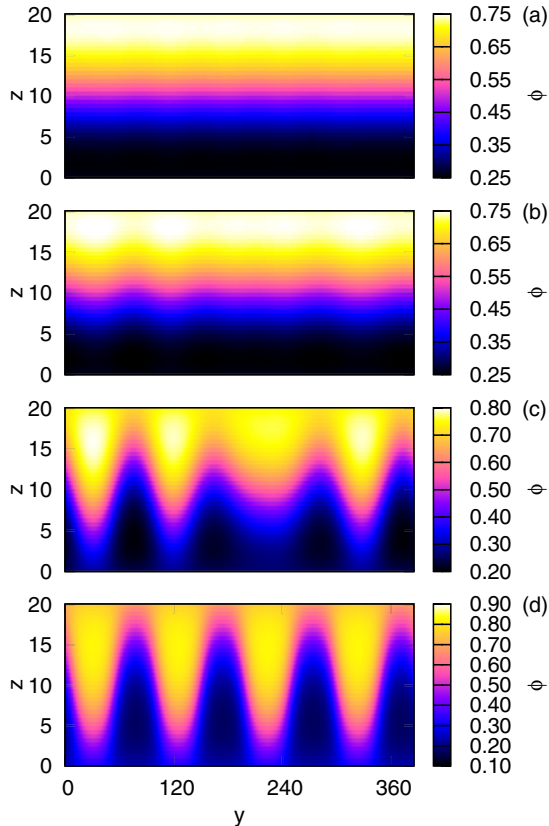


FIG. 14. (Color online) Simulation snapshots for $\chi = 0.026$ ($\chi > \chi_w$), $d = 20.1$, and antisymmetric walls ($\Delta z = 0.50$ and $\Delta \tau = 1.0 \times 10^{-5}$). (a) Metastable bilayer state ($\tau = 150$); (b) rupture of coexisting A-rich and B-rich layers of bilayer, coupled with bifurcation of ϕ at both walls ($\tau = 1300$); (c) continued rupture of layers distorts interface towards the walls, since the wall boundary conditions must be satisfied ($\tau = 2500$); (d) the boundary conditions of the laterally segregated states are met ($\tau = 4500$).

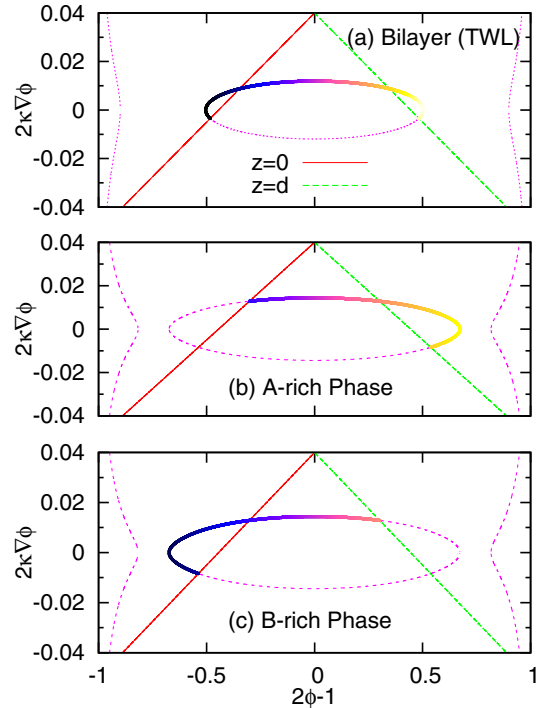


FIG. 15. (Color online) 1D phase portraits for equilibria in Fig. 14 (antisymmetric walls). (a) Metastable bilayer (TWL) ($\lambda = 0$, $\mathcal{H} = 0.000752$); coexisting phases ($\lambda = -\mu_{sim} = 0$): (b) A-rich phase ($\mathcal{H}_A = 0.000899$); and (c) B-rich phase ($\mathcal{H}_B = 0.000899$). Since $\lambda = 0$ the phase portraits are symmetric around $\phi = 0.5$. The bilayer trajectory passes through $\nabla \phi = 0$ near each BC, while the A-rich (B-rich) trajectories pass through $\nabla \phi = 0$ only near the A-attracting (B-attracting) wall BC at $z = d$ ($z = 0$).

lateral inhomogeneities at these stationary points, although the wall boundary conditions ensure that lateral inhomogeneities simultaneously grow at the walls. However, it certainly appears that rupture of the film proceeds from the stationary points near the surfaces. Inspection of the phase portraits of Fig. 15 shows that in order for the film to laterally separate, not only does the volume fraction at the confining walls have to undergo bifurcation, but one of the stationary points needs to disappear: for the *A*-rich (*B*-rich) phase, the stationary point near the *A*-attracting (*B*-attracting) wall is preserved and enriched in *A*-material (*B*-material), while the other stationary point disappears exactly where the *B*-rich (*A*-rich) phase forms; the enrichment and removal of a stationary point happens at the same depth, so we see lateral phase separation occurring at the stationary points, causing a distortion of the interface towards the walls where the stationary points disappear. Also, for lateral phase separation to occur, the required change in the profiles at the walls is much less than the change required at the stationary points, and while it is clear that lateral phase separation at the walls is inherent in this process, as film thickness is increased the stationary points in the trajectories can pass arbitrarily close to fixed points in the phase space (these fixed points are located at $\nabla\phi = 0$ between the gaps in

the Hamiltonian flows), meaning that the amount of the film profile constituting a stationary point can become arbitrarily thick.

It should be noted that the final state of Fig. 14 does indeed contain the laterally coexisting phases shown in the phase portraits of Fig. 15, and does not simply show an oscillatory interface. Lateral phase separation in antisymmetric films is in fact the transition from a delocalized interface (bilayer state) to an interface bound to one of the walls (laterally coexisting states) [22,23]. In Sec. VI A (Fig. 19), we show that the lateral domains of Fig. 14 will evolve into wider trapezoidal phases [24] when a noise term is included in the simulation.

For a film between symmetric walls, shown in Fig. 16, the TWL that forms first is actually a trilayer structure. It is clear that lateral phase separation occurs when the central layer ruptures. The phase portraits of Fig. 17 show that this rupture again occurs at a stationary point in the profile, where $\nabla\phi = 0$. The rupture of the central layer preserves the *A*-rich stationary point of the trilayer for the *A*-rich phase, and columns of *B*-rich phase form in the depleted regions caused by the enrichment of the *A*-rich stationary points.

C. Bypassing the wetting layer

If the dynamics of lateral phase separation via a transient wetting layer are ultimately controlled by wall-blend interactions (via boundary conditions enforced by the walls), then it should be possible to manipulate the dynamics in the film by attempting to control behavior at the confining walls. Here, we recommend a method that may prove useful in obtaining a laterally segregated state in polymer thin films: in the case of our asymmetric confinement (*B*-attracting wall at $z = 0$, neutral wall at $z = d$), if the *B*-attracting wall could be turned off temporarily to become a

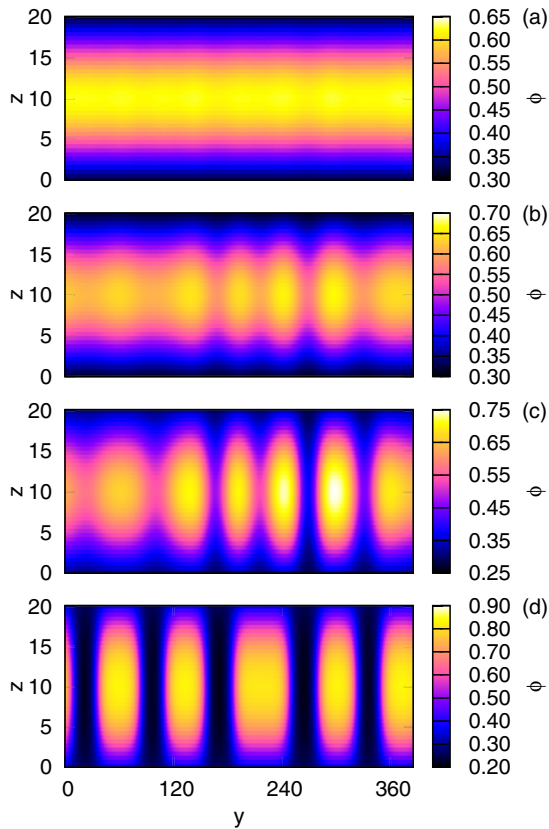


FIG. 16. (Color online) Simulation snapshots for $\chi = 0.026$ ($\chi > \chi_w$), $d = 20.1$, and symmetric walls ($\Delta z = 0.50$, $\Delta\tau = 1.0 \times 10^{-5}$). (a) Metastable trilayer state ($\tau = 50$); (b) *A*-rich (central) layer begins to phase separate, causing corresponding changes in ϕ throughout the trilayer ($\tau = 300$); (c) rupture of the *A*-rich layer once bifurcation of ϕ at the walls is sufficient ($\tau = 450$); (d) stable laterally segregated coexisting states ($\tau = 1000$).

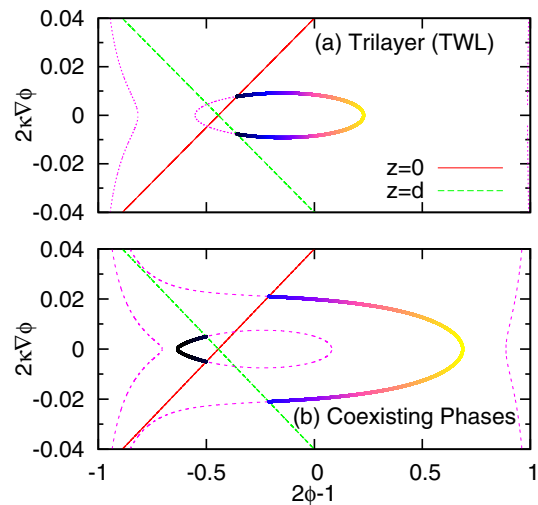


FIG. 17. (Color online) 1D phase portraits for equilibria in Fig. 14 (symmetric walls). (a) Metastable trilayer (TWL) ($\lambda = -0.000750$, $\mathcal{H} = 0.000968$); (b) coexisting phases ($\lambda = -\mu_{sim} = -0.001204$): *A*-rich phase ($\mathcal{H}_A = 0.001922$) and *B*-rich phase ($\mathcal{H}_B = 0.001092$). In all cases, $\nabla\phi = 0$ is located exactly in the center of the film.

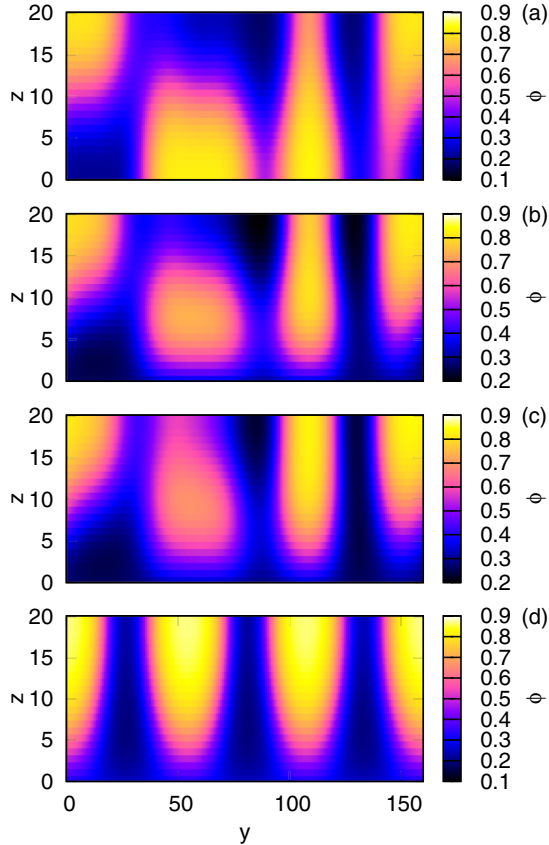


FIG. 18. (Color online) Simulation snapshots for $\chi = 0.026$ ($\chi > \chi_w$), $d = 20.1$, and asymmetric walls ($\Delta z = 0.84$, $\Delta\tau = 1.0 \times 10^{-4}$). Both walls are initially neutral, then the $z = 0$ wall is “turned on” (film becomes asymmetric) at $\tau = 160$. (a) Bulklike separation, with domains aligned to walls to satisfy BCs requiring $\nabla\phi = 0$ ($\tau = 150$); (b) moments after $z = 0$ wall is turned on ($\tau = 160$); (c) rapid evolution towards the coexisting states of the asymmetric film ($\tau = 170$); (d) laterally segregated state ($\tau = 300$) is reached an order of magnitude faster than via a transient wetting layer.

neutral wall, then we should suppose for a near critical mixture that a transient wetting layer will not form (in a noncritical blend $\phi \neq 1/2$, layering parallel to the walls may sometimes still occur [2]). If we then turn on the wall, we may obtain the laterally segregated state without having formed a bilayer first.

Figure 18 demonstrates that this may work in practice. When both walls are turned off [subfigure (a)], we see phase separation into domains with $\nabla\phi = 0$ (required for neutral walls). There are (in terms of 1D equilibria) two values of ϕ^{TWL} at each wall. The $z = 0$ wall is turned on to attract B material at $\tau = 160$ in subfigure (b) (asymmetric wall configuration) and there is immediate preferential attraction of B material to the $z = 0$ surface. However, ϕ_0^A and ϕ_0^B have been obtained, rather than ϕ_0^{TWL} . The TWL has been avoided and the film can evolve directly towards the laterally segregated state, shown in subfigure (d), and lateral segregation is achieved an order of magnitude faster than via a TWL. In solvent evaporation experiments, it might be possible to use this mechanism by choosing a solvent to adjust the wall-blend interactions.

VI. DISCUSSION

A. Random noise

The absence of a random noise term in our simulations, although maintaining clarity in our results, is why many lateral phases do not become more macroscopic at very late times (e.g., Fig. 14 does not show the wide trapezoidal-shaped coexisting phases expected at long times [24] although such trapezoidal shaped phases are simply wide versions of the phases shown), although this consideration is of little practical relevance in many experiments including solvent evaporation. Figure 19 shows a simulation for antisymmetric walls in which a continuous noise (consisting of Gaussian white noise with mean zero and amplitude (width) 0.01, in the form of random thermal currents, giving an additional contribution to Eq. (23) of $\nabla \cdot J^*(z, y, t)$ as in Ref. [24]). We see that a bilayer still forms and breaks up via the mechanism we have already presented. There are smaller scale lateral variations at the surface initially, and wider domains form at later times. Figure 19 appears to reproduce a contact angle appropriate for an antisymmetric film. We do not find that the

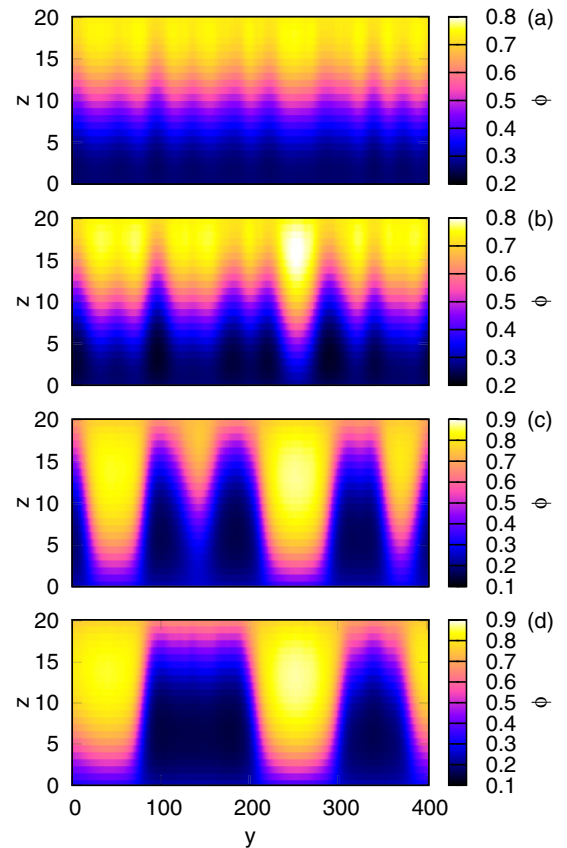


FIG. 19. (Color online) Simulation snapshots for $\chi = 0.026$ ($\chi > \chi_w$), $d = 20.1$, and antisymmetric walls ($\Delta z = 0.84$, $\Delta\tau = 1.0 \times 10^{-4}$). Random noise is included at every time step. (a) The bilayer interface is heavily distorted ($\tau = 25$); (b) lateral A -rich phase begins to form as the A -rich layer of the bilayer ruptures ($\tau = 125$); (c) A -rich phase retreats from B -attracting wall ($z \approx 150$) and neighboring A -rich phases grow ($\tau = 2225$); (d) macroscopic trapezoidal domains form at longer times ($\tau = 5000$). These phase equilibria match those in Figs. 14 and 15.

$A(B)$ -attracting surface is coated by $B(A)$ -rich material, as is sometimes suggested by schematic representations (the phase portraits of Fig. 15 support this; the $A(B)$ -rich trajectories *must* pass through $\phi = 0.5$ near the $B(A)$ -attracting wall for antisymmetric films, which agrees with the idea that these coexisting phases have an interface “bound” to one of the walls [22,23]).

B. Solvent evaporation

Many practical applications using polymer films involve solvent evaporation. Here we discuss the implications of our model, which could be easily extended to include solvent, for experiments involving solvent evaporation. We do this because our model reproduces and explains many phenomena without needing to include solvent. We suggest that solvent may influence lateral phase separation in several ways: (i) fast solvent evaporation provides lateral inhomogeneities in the transient wetting layer, which provide a kinetic route to the laterally segregated state that is often not reached (our simulations and frozen out-of-equilibrium states found in experiments [25] show strong resemblances); (ii) solvent evaporation allows phase separation to occur at the top surface which proceeds into the film [26], the solvent providing increased miscibility which prevents bilayer formation (the equilibria of ternary polymer-polymer-solvent films are analogs of equilibria for binary polymer-polymer films [27]); and (iii) overall reduction of solvent causes phase separation, and lateral phase separation occurs in stages that appear to match our simulations, with high, medium, and low solvent concentrations corresponding to a bilayer, a bilayer with a distorted interface, and a laterally segregated state, respectively [28]. A Marangoni-like instability has been suggested to explain the distortion of the bilayer interface prior to lateral phase separation [10,12,28], although we have shown that the intrinsic instability of the bilayer and surface bifurcation is

sufficient to cause distortion of the interface. Therefore we should consider that the phase equilibria of polymer films and the surface bifurcation mechanism we have presented here might be responsible for the film evolution seen in many experiments.

VII. CONCLUSION

We have derived a diffusion equation describing a binary polymer blend confined between two preferentially attracting walls or surfaces. We compared the phases produced in our simulations with profiles calculated using a 1D Hamiltonian phase portrait method to show that our diffusion equation correctly reproduces continuum behavior and that all of the equilibria that arise in two dimensions are simply 1D coexisting phases, existing in two dimensions under an altered chemical potential due to the lateral interfaces between these coexisting phases. We also show how the film profile is pinned at the film walls by effective boundary conditions.

We have identified the dynamics of lateral phase separation via a transient wetting layer for several wall-blend interaction configurations, showing that distortion of the interface in the transient wetting layer is coupled to changes in the film profile at the walls. The instability of the bilayer (below the wetting temperature) as a whole is not the same as an instability in the interface of the bilayer; in all cases we have studied, the growth of lateral inhomogeneities at the walls limits and dictates the dynamics. We have explained the dynamics with a “surface bifurcation mechanism”: the pinning of the profile at the film walls by effective boundary conditions imposed by the walls means that the film must undergo bifurcation of the profile at the walls in order to laterally phase separate into coexisting phases. The distortion of the interface in the wetting layer coincides with phase separation at the surfaces. Since our results should also extend to ternary blends, we discussed how solvent evaporation may assist our proposed mechanism.

-
- [1] S. Coveney and N. Clarke, *Phys. Rev. Lett.* **111**, 125702 (2013).
 - [2] R. C. Ball and R. L. H. Essery, *J Phys.: Condens. Matter* **2**, 10303 (1990).
 - [3] R. A. L. Jones, L. J. Norton, E. J. Kramer, R. J. Composto, R. S. Stein, T. P. Russell, A. Mansour, A. Karim, G. P. Felcher, M. H. Rafailovich, J. Sokolov, X. Zhao, and S. A. Schwarz, *Europhys. Lett.* **12**, 41 (1990).
 - [4] S. Puri and K. Binder, *Phys. Rev. A* **46**, R4487 (1992).
 - [5] G. Brown and A. Chakrabarti, *Phys. Rev. A* **46**, 4829 (1992).
 - [6] J. F. Marko, *Phys. Rev. E* **48**, 2861 (1993).
 - [7] S. Puri and K. Binder, *Phys. Rev. E* **49**, 5359 (1994).
 - [8] W. Straub, F. Bruder, R. Brenn, G. Krausch, H. Bielefeldt, A. Kirsch, O. Marti, J. Mlynek, and J. F. Marko, *Europhys. Lett.* **29**, 353 (1995).
 - [9] S. Y. Heriot and R. A. L. Jones, *Nat. Mater.* **4**, 782 (2005).
 - [10] P. M. Tabari, M. Geoghegan, J. R. Howse, S. Y. Heriot, R. L. Thompson, and R. A. L. Jones, *Eur. Phys. J. E: Soft Matter* **33**, 283 (2010).
 - [11] S. Coveney and N. Clarke, *J. Chem. Phys.* **137**, 174901 (2012).
 - [12] M. Souche and N. Clarke, *J. Chem. Phys.* **131**, 244903 (2009).
 - [13] P. G. de Gennes, *J. Chem. Phys.* **72**, 4756 (1980).
 - [14] H. Nakanishi and P. Pincus, *J. Chem. Phys.* **79**, 997 (1983).
 - [15] I. Schmidt and K. Binder, *J. Phys.* **46**, 1631 (1985).
 - [16] R. Pandit and M. Wortis, *Phys. Rev. B* **25**, 3226 (1982).
 - [17] J. W. Cahn, *J. Chem. Phys.* **66**, 3667 (1977).
 - [18] I. C. Henderson and N. Clarke, *Macromol. Theory Simul.* **14**, 435 (2005).
 - [19] J. I. Fukuda, M. Yoneya, and H. Yokoyama, *Phys. Rev. E* **73**, 066706 (2006).
 - [20] M. Müller, K. Binder, and E. Albano, *Europhys. Lett.* **50**, 724 (2000).
 - [21] See Supplemental Material at <http://link.aps.org/supplemental/10.1103/PhysRevE.89.062603> for animations of the simulation figures.
 - [22] A. Parry and R. Evans, *Phys. Stat. Mech. Appl.* **181**, 250 (1992).

- [23] K. Binder, *Annu. Rev. Mater. Res.* **38**, 123 (2008).
- [24] S. K. Das, S. Puri, J. Horbach, and K. Binder, *Phys. Rev. E* **72**, 061603 (2005).
- [25] S. Walheim, M. Bo, G. Krausch, and U. Steiner, *Macromolecules* **30**, 4995 (1997).
- [26] G. A. Buxton and N. Clarke, *Europhys. Lett.* **78**, 56006 (2007).
- [27] M. Souche and N. Clarke, *Macromolecules* **43**, 5433 (2010).
- [28] A. D. F. Dunbar, P. M. Tabari, A. J. Parnell, S. J. Martin, M. W. A. Skoda, and R. A. L. Jones, *Eur. Phys. J. E: Soft Matter* **31**, 369 (2010).